Supporting Information

Brodland et al. 10.1073/pnas.1006591107

SI Text

Calculation of the Passive Forces. For any given time step i, the finite element code is used to calculate the damping matrix $\mathbf{C}_i$ associated with the viscosity μ and the geometry of the system at that time (1). The observed displacements of each of the registration points, which for convenience are chosen to correspond to the finite element nodes, are used to construct the velocity vector $\dot{\mathbf{u}}_i$. To determine the global forces $\mathbf{f}_i$ that must act during the time interval Δt_i between successive time-lapse images to generate these displacements, the matrix product

$$\mathbf{C}_i\dot{\mathbf{u}}_i = \mathbf{f}_i \qquad [S1]$$

is formed. These are the forces shown in Fig. 1*C* of the main article.

Calculation of the Active Forces. Forces from contraction of cortical actomyosin networks, cell membrane tension, cell adhesion forces, and stress fibers are assumed to be resolvable into equivalent tensions along specified directions and to drive the deformation of the passive components. If these line segments are chosen to align with known cytoskeletal elements and the morphology is sufficiently simple, the calculated forces can be interpreted easily, often in terms of specific cytoskeletal components, as in the main article. The discrete regions chosen for the analysis need not correspond to cells, but could be regions of arbitrary geometry as suggested by Figs. 1–3 (main article). In the present model, regions were chosen to correspond generally to cells, but regions comprising up to four cells and regions containing only a portion of a cell were also used. The radial forces shown in multicell elements are those generated by all of the cells in that region. (The radial forces reported in Fig. 3 are normalized to circumferential length so that their colors do not change if the regions are made multiple cells wide.) The circumferential forces are the mean of those acting in each cell within that region. Cells at the junction of the mesoderm and ectoderm develop strongly curved geometries in vivo. So that the model regions could do the same, these cells were broken into quadrilateral elements that were stacked in the apical–basal direction. Based on foreknowledge of the cell cytoskeleton, driving forces were assumed to act parallel to the curved cell–cell boundaries.

If the tensions t_{ij} acting along each line segment j during time interval i were known, it would not be difficult to resolve them into their x and y components using direction cosines and thereby calculate the net global forces from edge tensions $\mathbf{f}_i^{(T)}$, like those shown in Fig. 1*C*. Coupling between the forces at each node arises because each edge tension contributes to the forces at two nodes. At each time step, the tensions t_{ij} are represented by the vector $\mathbf{t}_i$. The relationship between the line forces $\mathbf{t}_i$ and $\mathbf{f}_i^{(T)}$ can be written as

$$\mathbf{G}_i^{(T)}\mathbf{t}_i = \mathbf{f}_i^{(T)}, \qquad [S2]$$

where the rectangular matrix $\mathbf{G}_i^{(T)}$ is called the tension geometric matrix. Pressure forces are also assumed to be present in each cell, and their contributions to the nodal forces are calculated according to the approach of ref. 2 and written in terms of a pressure geometric matrix $\mathbf{G}_i^{(P)}$. When the unknown pressures in each cell are assembled into the vector $\mathbf{p}_i$, the net global forces from cell pressures $\mathbf{f}_i^{(P)}$ are calculated by

$$\mathbf{G}_i^{(P)}\mathbf{p}_i = \mathbf{f}_i^{(P)}. \qquad [S3]$$

Both geometric matrices must be recalculated at each time step i so as to reflect the current geometry. In practice, Eqs. **S1** and **S2** are composited into a single matrix equation

$$[\mathbf{G}_i^{(T)}|\mathbf{G}_i^{(P)}]\left\{\frac{\mathbf{t}_i}{\mathbf{p}_i}\right\} = \mathbf{f}_i^{(T)} + \mathbf{f}_i^{(P)} = \mathbf{f}_i \qquad [S4]$$

or

$$\mathbf{G}_i\mathbf{T}_i = \mathbf{f}_i,$$

which is solved to simultaneously determine the edge tensions $\mathbf{t}_i$ and cell pressures $\mathbf{p}_i$ that must act at time step i to produce the observed displacements $\mathbf{u}_i$ from Eq. **S1**. The full geometric matrix $\mathbf{G}_i$ comprises both the tension and pressure geometric matrices. The unknown tensions and pressures are collected into the vector $\mathbf{T}_i$ to achieve a compact notation.

In general, the inverse problem implied by Eq. **S4** is poorly conditioned and susceptible to noise from sources such as image capture and digitization errors. Because the regions used in the present study were approximately rectangular in shape, a pressure correction step was also employed. To produce stable solutions and reduce noise effects, an adaptive weighted least squares approach was used to combine information from neighboring time steps. Given a total of n time steps, the system to estimate the unknown tensions and pressures at time step i was written

$$\sum_{k=1}^{n}[\lambda_i^{|i-k|}\mathbf{G}_k\mathbf{T}_i] = \sum_{k=1}^{n}[\lambda_i^{|i-k|}\mathbf{f}_k], \qquad [S5]$$

where information from neighboring time steps k was weighted with the exponentially decaying weight λ_i. This approach is similar to a recursive least squares formulation with forgetting factor, but the weighting is applied noncausally (i.e., to past and future time steps). The weighting factor λ_i can be prescribed for the entire history of the patch, or can be determined using a variable formulation, similar to the variable forgetting factors of refs. 3–5. The algorithm and its associated code were verified using a wide range of noisy synthetic data. Displacement data were smoothed using a Savitzky–Golay filter having window size 9 and smoothing order 2 before being passed to the inversion step, where λ was set to 0.5. The intracellular pressures and yolk pressures were set to zero in the inversion step and subsequently adjusted to eliminate any negative tensions along the apical and basal cell surfaces. If the yolk were pressurized, the edge tensions would be positively offset compared to those reported here.

Algorithm Validation. A series of tests were carried out to evaluate the quality of the video force microscopy (VFM) output and the ability of VFM to reveal subtle force details. To this end, a circumferential reference system in which the coordinates deform with the material (i.e., a Lagrangian frame) was established (Fig. 2*A*). Fig. 4 shows that the forces in the ectoderm and mesoderm vary according to well-defined, tissue-specific profiles during ventral furrow formation. The curves produced by VFM are feature rich, closely spaced, smoothly ordered, and self-consistent, suggesting that the outputs are reliable and reasonably error-free. The curves demonstrate that VFM has the power to elucidate important spatial and temporal details about the forces that drive tissue reshaping.

Synchronization of Embryos. Images from different genotypes were synchronized based on the time that the cells at the dorsal midline reached their maximum apical-basal height (dimension b in Fig. 2*B*) as they complete cellularization. Importantly, this proved a reproducible timer that was independent of events occurring within the ventral furrow. As shown in Fig. S1, the peak was well-defined in all genotypes considered in the study. Peak heights occurred simultaneously throughout the mesoderm but not the ectoderm (Fig. S2).

Force versus Myosin II Correlation. Figure S3 shows edge forces as calculated by VFM versus myosin II levels. The latter were determined as the average of the pixel intensities in the original 16-bit image along a 10-pixel-wide band centered on each apical and radial edge in the mesoderm. Basal edges were not considered because much of the myosin II present appears to be related to cellularization. The averaging areas were made two pixels shorter than their corresponding region edges so as not to pick up false information from adjacent transverse lines. Shown in blue are data from the left side of the embryo over all of the images except the first two, because the intensity scale in those images appeared different compared to the rest. Fewer data points were included from later images because many of the region edges became shorter than 2 pixels long. The apical data show a correlation between myosin II concentration and VFM force (black line).

1. Brodland GW, Viens D, Veldhuis JH (2007) A new cell-based FE model for the mechanics of embryonic epithelia. *Comp Met Biomech Biomed Eng* 10:121–128.
2. Viens D, Brodland GW (2007) A three-dimensional finite element model for the mechanics of cell-cell interactions. *J Bio Mech Eng* 129:651–657.
3. Fortescue TR, Kershenbaum LS, Ydstie BE (1981) Implementation of self-tuning regulators with variable forgetting factors. *Automatica* 17:831–835.
4. Lin J-W, Betti R (2003) On-line identification and damage detection in non-linear structural systems using a variable forgetting factor approach. *Earthq Eng Struct D* 33:419–444.
5. Paleologu C, Benesty J, Ciochina S (2008) A robust variable forgetting factor recursive least-squares algorithm for system identification. *IEEE Signal Proc Let* 15:597–600.

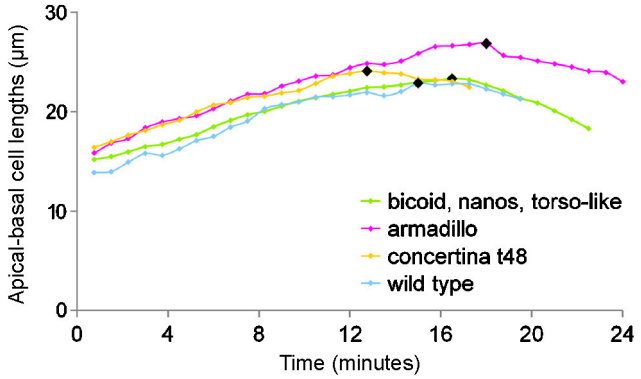

Fig. S1. Genotypes were synchronized according to the time (marked with a diamond) at which the apical-basal heights of the most dorsal cells were maximized.

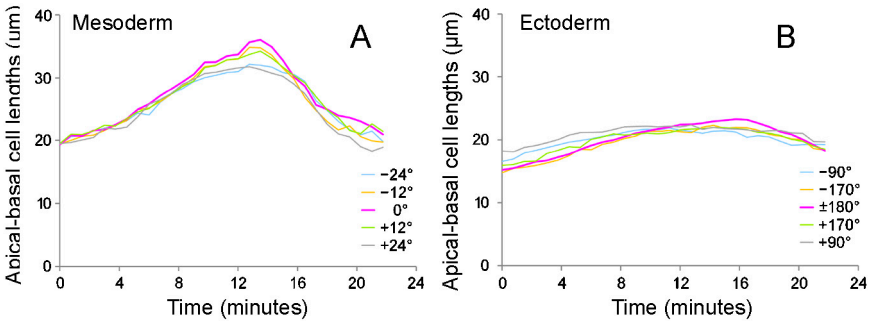

Fig. S2. Apical-basal cell heights versus time. Heights are shown for the mesoderm (*A*) and ectoderm (*B*). The angular positions at which the cell heights were measured are reported in terms of the coordinate system shown in Fig. 2*A*.

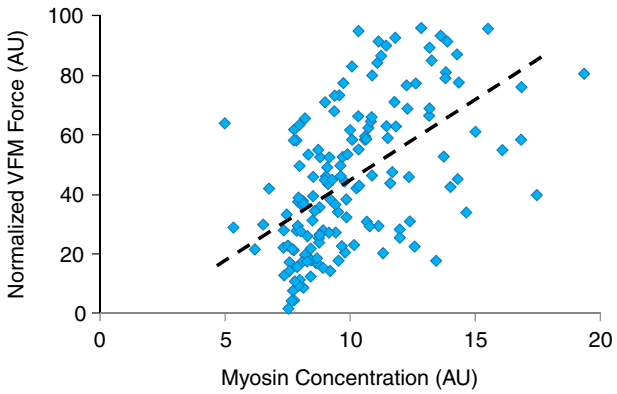

Fig. S3. VFM force versus myosin II concentration. Blue squares correspond to apical edges of the mesoderm on the left side of the embryo (−40 to 0° in Fig. 2*A*), and the black line is a best fit to those points. A consistent positive correlation is observed.

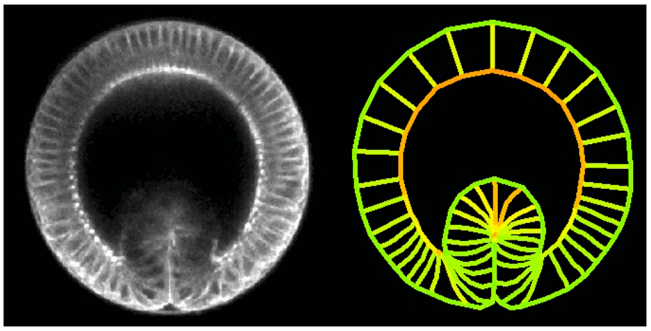

Movie S1. Multiphoton images of a WT embryo expressing Sqh (myosin II)-GFP are shown side by side with a graphic representation of its VFM results. Images were collected every 45 s.

Movie S1 (AVI)

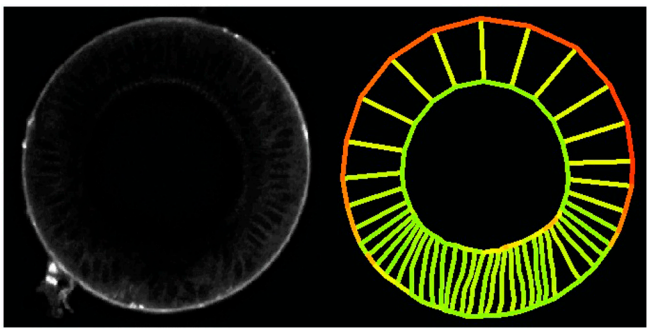

Movie S2. An *armadillo* embryo and its VFM results.

Movie S2 (AVI)

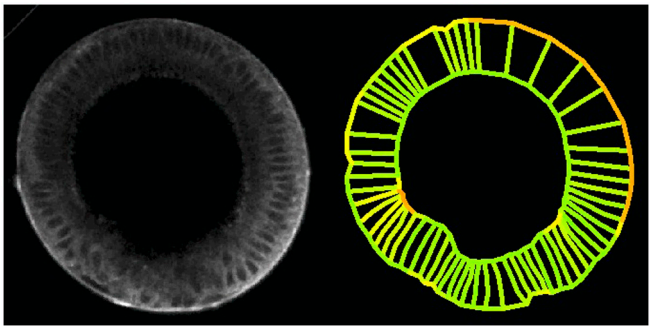

Movie S3. A *concertina;t48* embryo and its VFM results.

Movie S3 (AVI)

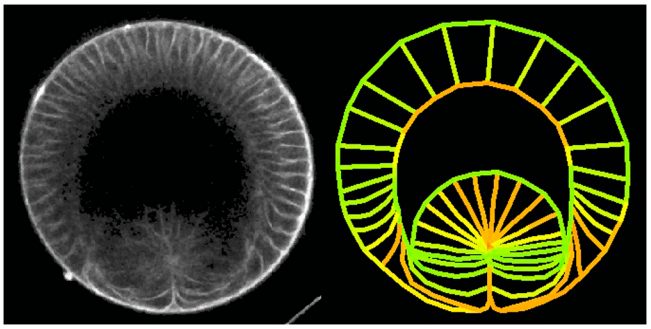

Movie S4. A *bicoid nanos torso-like* embryo and its VFM results.

Movie S4 (AVI)